

Comparative Characterization of Petrophysical and Mechanical Properties of Siliciclastic Reservoir Rocks within a compressional structure of the Teapot Dome Oilfield, Wyoming, USA

Rotimi Oluwatosin John^{*1}, Ogunkunle Fred Temitope¹, Onuh Charles, Yunusa¹, Ameloko Adujo Anthony¹, Enaworu Efeoghene², Ekeledo Ifeoma Faith¹, and Gospel Chinwendu Amaechi³

¹*Petroleum Reservoir and Production Technology Research Group (PRPTRG), Petroleum Engineering Department, Covenant University, Ota, Ogun State, Nigeria*

²*School of Geography, Geology and the Environment, University of Leicester, UK.*

³*Department of Geology, University of Ibadan, Nigeria.*

Received 19th May, 2020, Accepted 22nd July, 2020

DOI: 10.2478/ast-2020-0009

*Corresponding author

Rotimi Oluwatosin John E-mail: rotimioohjay@gmail.com, tossynrotimmy@yahoo.com

Tel: +234-8183388280

Abstract

Working with subsurface engineering problems in Hydrocarbon exploration as regard rock elastic and petrophysical properties necessitate accurate determination of in-situ physical properties. Several techniques have been adopted in correlating log-derived parameters with petrophysical and mechanical behavior of the rocks. However, limited field applications show there are no particular parameters and correlations that are generally acceptable due to the regional variation in geologic features (i.e., degree of mineralogy, texture, etc.). This study presents a method that assesses the disparity in petrophysical properties of oil and gas reservoir rocks in relation to their elastic/mechanical properties from 10 well-logs and 3D migrated seismic data. Two distinct facies were identified from seismic data after computing attributes. Reflection strength attribute of 2.5 and above depicts Bright spots within the central section of the field as clearly revealed by Variance and Chaos attributes. Formation properties calculated from logs were conformally gridded in consonance with the reflection patterns from the seismic data. The average Brittleness index (BI) of 0.52 corresponds to Young's modulus (E) values of between 8 and 16 for the dense portion. This portion is the laminated, reasonably parallel, and undeformed part, flanked by the unlaminated and chaotic zones. From cross plots, the distinguished lower portion on the plot is the segment with higher sand of more than 50 %. This segment corresponds to the reservoir in this study as confirmed from the genetic algorithm neural network Acoustic impedance inversion process result. Similarly, the plot of Compressional velocity (V_p) and Poisson's ratio (ν), reveals the laminated sand value of not less than 0.32 of ν , and V_p of about 4.2 km/s. The average porosity is about 16 %, average water saturation is about 16 %, and average permeability is approximately 25 md. Rock properties trends in a unique pattern and showing fluctuation that confirms the compressive nature of the structure with corresponding petrophysical properties. This trend is sustained in permeability computed and suggests a significant gravity-assisted compaction trend and fluid movement. It gives a reasonable idea of the fluid movement interplay and mechanical property variation within the sequence and across the dome. This part probably has been subjected to fair compressional deformational forces initiated from outside the survey.

Keywords: Seismic attributes, seismic inversion, Permeability, Bright spots, Brittleness index, Acoustic impedance



1.0 Introduction

The rise in demand for more oil and gas even in the face of drop in oil price has caused companies to want to maximize the field potentials and reduce costs associated with production of oil and gas. Meeting these demands in well productivity requires little or no restriction in terms of production rate and also keeping up with sand production below threshold limits. Predicting or avoiding sanding risk necessitates the understanding of rock mechanical properties such as the Poisson's ratio, young's modulus, bulk modulus, and shear modulus. These rock elastic properties are fundamental in the evaluation of the lifecycle of oil and gas fields. They are equally crucial in geomechanical applications, most essentially where the understanding of sand production, hole stability analysis, hydraulic fracturing, and casing design is critical.

However, the ability to accurately and precisely estimate these elastic properties during drilling and production is somewhat challenging to the Petroleum Engineers and Petroleum Geologist. The elastic properties can be experimentally evaluated (static properties) using the stress-strain response of core samples under uniaxial compression, but this is highly time-consuming and sometimes, could be complicated. With the advent of new technologies in computing, some of the challenges in laboratory determination of rock elastic properties were overcome via new computing and experimental techniques. Some of which are even more faster than the conventional laboratory experiments. To bridge the time disadvantage of laboratory determination of rock elastic properties, alternative methods that utilize both theoretical and empirical approaches were introduced that relate elastic moduli with physical properties of the rock such as porosity and/or rock mineral composition. However, field applications show that there are no peculiar parameters and relations that can be adopted, as all these properties vary with region and location, even for the same rock type. Furthermore, most available experimental data are strictly for well-compacted rocks (limestones and well-cemented sandstones), simply because unconsolidated or friable sands are difficult to characterize because of coring (Onyeji et al., 2018). Nowadays, with the advent of improved technologies and robust interpretation algorithms, geophysical well logs techniques have been employed in estimating inherent rock and fluid properties of the reservoirs. It provides a non-destructive (dynamic properties), cost-efficient, real-time and covering most entire length of the well (the reservoir interval inclusive). Some of such logs that are frequently used by servicing companies include; Gamma-ray (GR), Density (DL), Neutron/Density log and Sonic log (Acoustic). All these logs possess the basic properties of rock formation such as shale content, porosity, saturation, density, and formation boundaries. The study is aimed at assessing the variation in petrophysical properties of hydrocarbon-bearing beds in relation to elastic/mechanical properties within different layered vertical sequences of the Teapot dome, Wyoming, USA.

Objectives are to characterize the different formations using seismic reflection patterns and specific attributes. Well-logs are also interpreted for formation tops and various continuous attributes

computed. An assessment of the diversity in petrophysical and elastic properties within the zone is made for formation stability in the light of production efforts.

These petrophysical properties are important for reservoir characterization, reserve estimation, and oil recovery. The mechanical properties like Young modulus, Bulk modulus, Shear Modulus, Poisson ratio, Acoustic Impedance, and Brittleness index were estimated from the density logs and velocity logs and are applied in wellbore stability, estimating mud window, predicting sand production and much more. Al-Kattan and Al-Ameri, (2012), estimated the mechanical properties of a field from conventional log data. The mechanical properties included formation strength, Poisson's ratio, Elastic, and Shear modulus. Results were correlated with depth and effective stress. Rock mechanical properties can be estimated indirectly from conventional wireline logs, primarily sonic, density, and gamma-ray logs.

Rock mechanical properties can be determined or measured using two methods; static and dynamic methods. Static methods involve the application of pressure on the rocks and are usually carried out in the laboratory with specific test equipment. Some of the tests carried out in the laboratory to determine static mechanical properties are Triaxial compression test, Unconfined compression test, hydrostatic test, Oedometer test, and so on. However, the static methods are difficult, expensive, and time-consuming (Fei et al., 2016). Dynamic methods on the other hand, make use of correlations and calculations of compressional wave velocities (V_p) and shear wave velocities (V_s), which can be obtained from well logs or the laboratory (Xu, et al., 2016). Acoustic well logging is one of the methods used to obtain or estimate dynamic mechanical properties of rocks as it is used to measure the acoustic wave velocities which can be used together with density to obtain dynamic Elastic modulus and dynamic Poisson ratio.

2.0 Experimental

Area of Study

The data used were obtained from the teapot field or Naval Petroleum Research #3 (NPR3) field in Natrona County, Wyoming. The teapot dome field or Naval petroleum reserve field is located in central Wyoming, about 37 miles north of Casper. NPR3 is a government-owned oil field operated by the Department of Energy through its Rocky Mountain Oil Testing Centre. NPR3 was created by President Wilson on April 30, 1915 from lands in the public domain and has an area of approximately 9400 acres (Ricardo, 2005; Friedmann and Stamp, 2006). Oil production in the teapot field is primarily from three formations; the shallow Shannon formation (400 ft - 1000 ft), the second wall creek member of the Frontier formation (2500 - 3000 ft), and the Teen sleep formation at 5500 ft. The sedimentary formations were found to have been deposited during the Cretaceous time (Chappelle, 1985; Nelson, 1962). The location map of the teapot dome field is shown in figure 1 with a basemap and 10 wells having varying offset distances. The location of the main interpreted seismic seed lines are also displayed in green, blue, and orange lines.

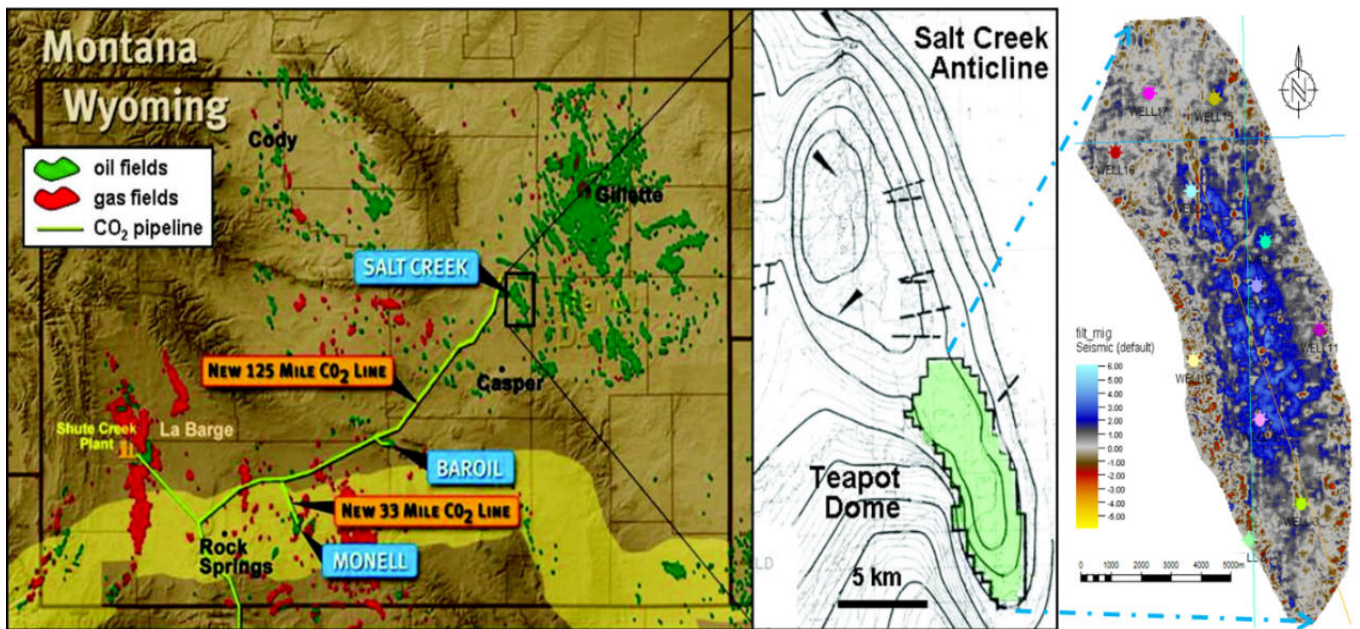


Figure 1: Location map of the teapot dome field with basemap, 10 wells and interpreted lines (modified after Friedmann and Stamp, 2006). Inline, crossline, and random lines are colored blue, green, and brown respectively on the survey.

Preliminary data for this study include wireline logs from ten wells. The well logs were available in Log ASCII (American Standard Code for Information Interchange) Standard (.LAS) format. The well logs were quality checked and a curve inventory was done to know the curves available for each well. 3D filtered migrated seismic data having 1501 samples per trace and 2 ms sampling interval with 533 lines was used. These provided insight into spatial subsurface properties.

Determination of Petrophysical Properties

Water saturation was calculated using the Indonesia Equation expressed as equation 3 below. In calculating water saturation, volume of shale and effective porosity are needed as input. Volume of shale calculations were done based on the gamma-ray method using the Larionov’s equation for older rocks which is equation 1. In calculating effective porosity, the shale distribution is inferred by plotting porosity against the volume of shale which showed a comprehensive shale distribution, visible and separated into structural, laminated, and dispersed, after Thomas and Stieber (1975) and Mkinga et al., (2020). The effective porosity equation for laminated shale distribution is shown in equation 2 below.

$$V_{sh} = 0.33(2^{(2 \cdot I_{gr})} - 1) \dots\dots\dots 1$$

$$\phi_e = \phi - (\phi * V_{sh}) \dots\dots\dots 2$$

$$\frac{1}{R_t} = \left[\frac{\phi_e^m}{a * R_w} + \frac{V_{sh}^{(1-0.5V_{sh})}}{R_{sh}} \right] * S_w^{0.5 * n} \dots\dots\dots 3$$

Indonesia equation:

Where; I_{gr} is the Gamma Ray index, V_{sh} is the volume of Shale, R_{sh} is shale resistivity, which was estimated to be approximately 2.24 Ωm at volume of shale of 0.99. R_i is true resistivity of formation from well logs. Cementation exponent (m) and saturation exponent (n) are conveniently assumed to be 2, tortuosity factor (a) was taken as 0.81. R_w was estimated using Pickett plot as 0.5302 Ωm (Krygowski, & Asquith, 2004). Permeability was estimated using Timur’s equation

which is expressed as equation 4 (Ellis and Singer, 2007; Zheng et al., 2015; Rotimi, et al., 2016).

$$K^{0.5} = 100 \frac{\phi^{2.26}}{S_{wi}} \dots\dots\dots 4$$

Timur’s (1968):

Where K is permeability in miliDarcies, Φ is porosity and S_{wi} is irreducible water saturation. The irreducible water saturation was taken to be approximately 0.4 based on research from Ricardo, (2005) and Chapelle, (1985).

Determination of Mechanical Properties

In determining mechanical properties of the reservoir, bulk density of the formation, compressional wave velocity, and shear wave velocity are vital rock elastic parameters that makes it possible.

Compressional wave velocity is gotten from the sonic log, Compressional wave Velocity (V_p) is the inverse of the interval travel time. However, shear wave travel time was not available, so it was estimated using popular correlations developed by Castagna & Greenberg, (1992). The correlations for estimating shear wave velocity in sandstone and shale formations are presented as equation 5 and 6 respectively:

$$V_s = (0.804 * V_p) - 0.856 \dots\dots\dots 5$$

$$V_s = (0.76969 * V_p) - 86735 \dots\dots\dots 6$$

Where V_s is Shear wave velocity in Km/s and V_p is Compressional Velocity in Km/s. The compressional wave velocity is simply the inverse of the travel time. The last two equation implies that a Volume of shale greater or equal to 40 %, equation 6 is applied in calculating Shear wave velocity. However, at a volume of shale less than 40 %, equation 5 is used in calculating the shear wave velocity. Porosity is an important parameter in carrying out volumetric analysis of reservoirs; it is a measure of how much fluid can be stored. Porosities usually range from 5 % to 60 % depending on the age (degree of

consolidation), packing arrangement, sorting and grain size (Bassiouni, 1994; Darling, 2005; Rotimi, et al., 2010). Reservoir porosities range from 0.03 to 0.48 across all wells.

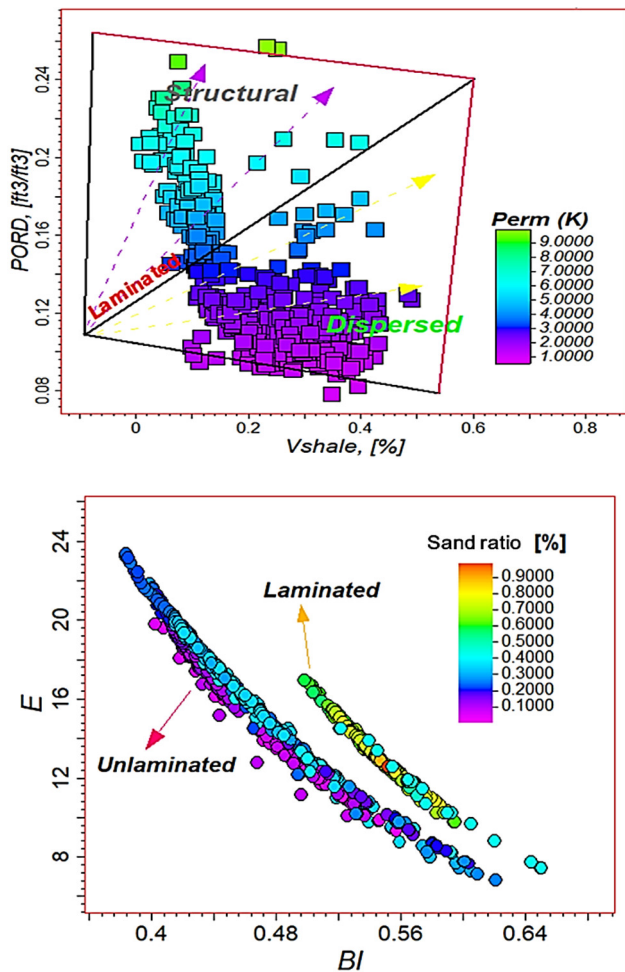


Figure 2: Top: modified Thomas-Stieber crossplot. Bottom: Crosplot of Young modulus (E) and Brittleness Index (BI) showing distinguished as laminated and unlaminated formations.

Mechanical properties that were evaluated in this study include; Young modulus (E), Poisson’s ratio (ν), Shear modulus (G), elastic moduli (λ), Bulk modulus (K), Acoustic Impedance (AI) and Brittleness Index (BI) using equations 8 to 14 (Edlmann, 1998; Memarian & Azizi, 2006). Poisson Ratio is a measure of the change in the shape of the reservoir rock under stress. According to Bentley and Zhang (2005), Poisson’s ratio is known to be between the ranges of 0 - 0.5. The higher the value the more likely the rock will change shape under stress (Xu, et al., 2016). Brittleness Index has no definite definition but has been used to classify shale into brittle or ductile shale, it is observed that the presence of quartz increases the brittleness index while the presence of clay significantly reduces the brittleness index (Fjaer et al., 2008). The significance of this is the perception that brittleness of a rock affects how the rock will fail or fracture during drilling and production operations. Young modulus (E) is a measure of a rocks stiffness and

resistance to uniaxial compression. A rock mass with high E is said to be stiff or rigid. Bulk modulus is the inverse of compressibility and is a measure of the incompressibility of a rock. A rock with high bulk modulus will be very incompressible and therefore have low compressibility (Terzaghi, et al., 1996; Jorg, et al., 2015; Fei, et al., 2016). From Table 1, this property increases with depth. The Lamé’s parameter relates stresses and strains in the perpendicular direction and is closely related to incompressibility. All these properties are presented in Table 1.

Comparison of E and BI via crossplot shows distinction in hard data. Separations seen corresponds to laminated and unlaminated (structural and dispersed) divisions (Figure 2). Computed hard data value for BI between 0.52 with corresponding E values of between 8 and 16 is the laminated, fairly parallel undeformed portion. Outside this distribution is the unlaminated delineation. Acoustic impedance relationship with E, crossplotted to show separations in sediment property association.

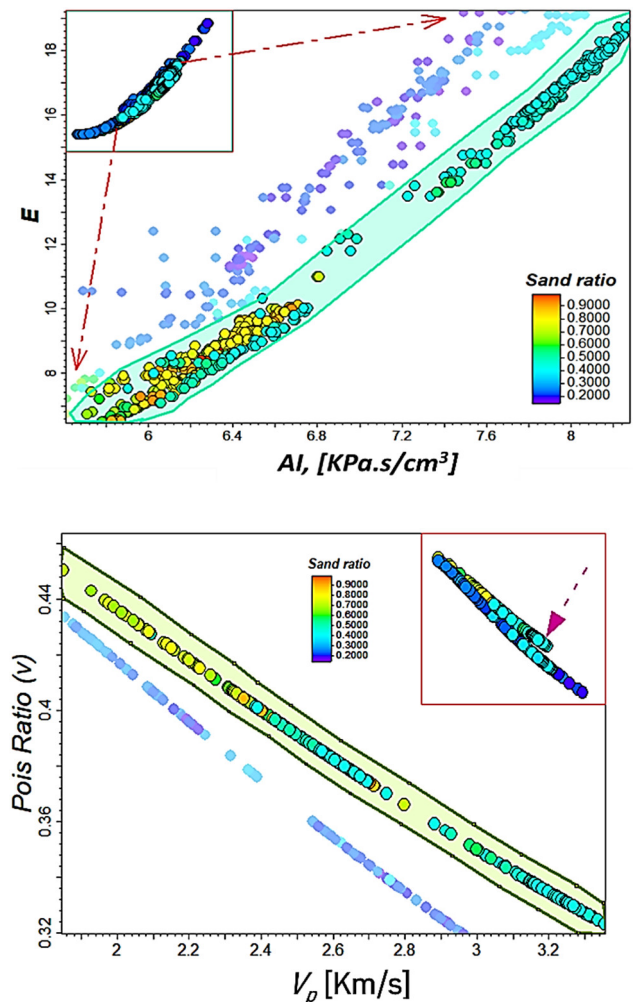


Figure 3: Top: Crossplot of E and AI. Bottom: Poisson’s ratio and Compressional velocity crossplot.

Figure 3 shows a lower and upper portion. The distinguished lower portion on the plot depicts the segment with higher sand of more than 50 %. This corresponds to the reservoir in this study. Similarly, plot of Compressional velocity (V_p) and Poisson's ratio (ν), reveals laminated sand value of not less than 0.32 on ν axis and V_p of about 4.2 km/s (figure 3).

$$\text{Shear modulus (G)} = \ell V_s^2 \dots\dots\dots 8$$

$$\text{Elastic moduli } (\lambda) = \ell V_p^2 - 2\ell V_s^2 \dots\dots\dots 9$$

$$\text{Poisson's ratio}(\nu) = \frac{V_p^2 - 2V_s^2}{2(V_p^2 - V_s^2)} \dots\dots\dots 10$$

$$\text{Young Modulus (E)} = \ell V_s^2 \frac{3V_p^2 - 4V_s^2}{V_p^2 - V_s^2} \dots\dots\dots 11$$

$$\text{Bulk modulus(K)} = \ell V_p^2 - \frac{4}{3} \ell V_s^2 \dots\dots\dots 12$$

$$\text{Acoustic Impedance (AI)} = \ell V_p \dots\dots\dots 13$$

$$\text{Brittleness Index (BI)} = \frac{100 \left(\frac{\nu - \nu_{\max}}{\nu_{\min} - \nu_{\max}} \right) + 100 \left(\frac{E - E_{\min}}{E_{\max} - E_{\min}} \right)}{2} \dots\dots\dots 14$$

These properties were computed across all wells and sampled to the interpreted formation as characteristic attributes for all correlation. Figure 4 shows correlation panel of 7 wells flattened on the first formation (horizon 1). The formations were identified based on signatures from GR log, Neutron-Density logs, Sonic log and Deep resistivity log presented on tracks 1 – 4 respectively. Surfaces were made using conformable gridding algorithm for all sand top identified. Surfaces were also built for all sampled attributes from which relationship variations were obtained and compared with seismic data.

Seismic Data

Operation on 3D migrated seismic data involves horizon tracking after achieving Sonic assisted calibration. The four horizons interpreted are conformable and follow the trough of wavelet sample on most trace. Seismic attributes computation attempted to relate spatial signal around a point; the location of the tracked horizon and various windows defined around it from where the respective attributes computation operations are done (Rotimi, et al., 2014a). In doing this, amplitudinal energy variation is compared as distributed from a trace to the adjoining trace on either the inline or crossline. Locations where characters of the resultant attribute changes become zone(s) of interest for further interpretation. Both stratigraphic and structural attributes were examined in this study.

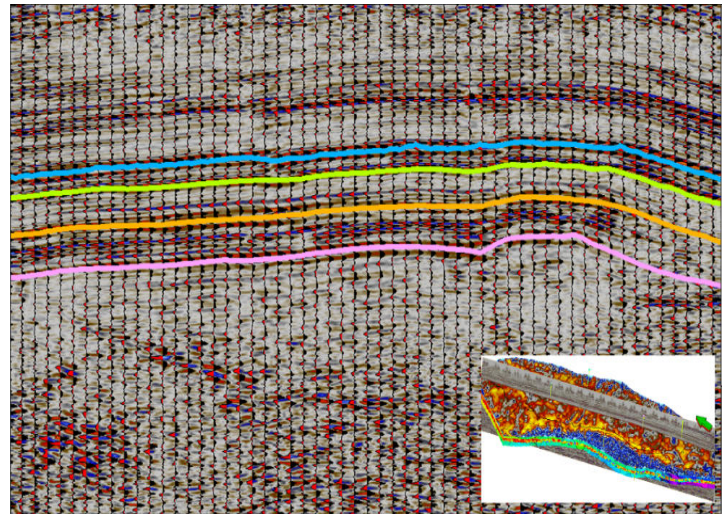


Figure 5: Trace wiggle overlain seismic random line with interpreted horizon. From top to base is horizon 1 – 4, is blue, green, orange, and pink lines, respectively.

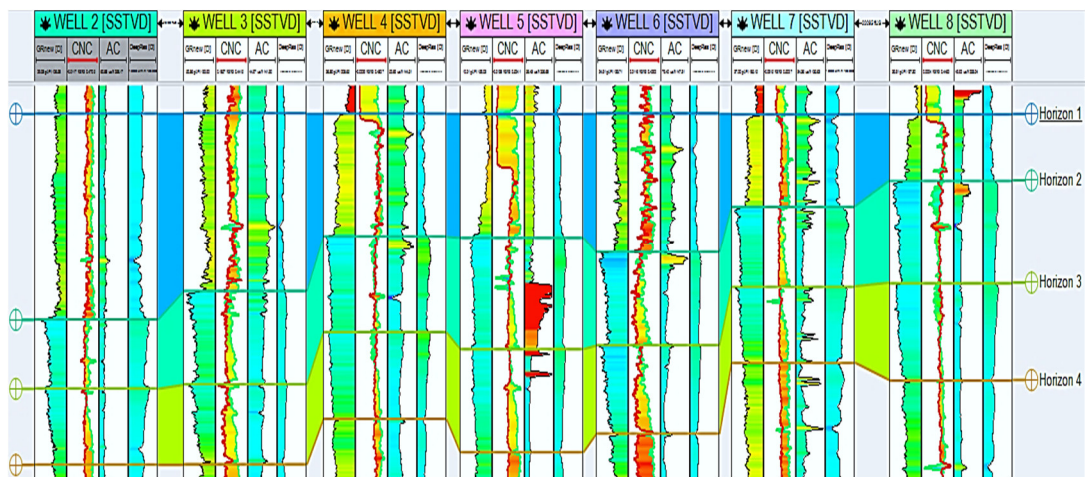


Figure 4: Correlation across wells and interpreted formations. GR log, Neu-Den crossplot, Sonic log, and Deep Resistivity logs are in tracks 1, 2, 3, and 4 respectively.

Attributes analysis

Reflectors, also known as interface in seismic data acquisition stores the energy that reflects wave pulse in the subsurface. The horizon and boundaries between overlying or underlying beds contain different energies and phase stores in the amplitude of wavelet arrivals as signals that are analyzed within a seismic trace. The reflection strength of a horizon carries the instantaneous energy or instantaneous amplitude.

This attribute is also called Envelope and it is mathematically expressed as the square root of real and imaginary component of the seismic. This attribute helps in detecting points of hydrocarbon accumulation termed bright spots (Rotimi, et al., 2010). This occurs as significant strong reflections caused by distinct lithological changes and sequence boundaries (Huang, et al., 2020). Chaos attribute computed around seismic trace assisted in highlighting zones of organization within the data. This property illuminates continuity in beds and otherwise. This is achieved by analyzing the change in signal properties with direction in a 3D space. Migration paths, structural elements, and textural variations are seen clearly on the output data.

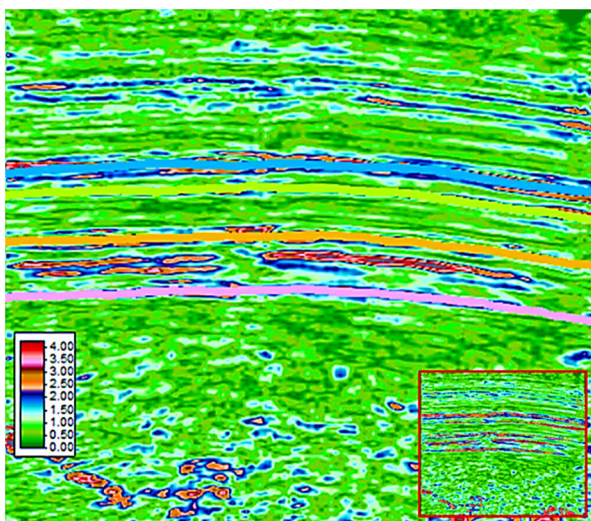


Figure 6: Reflection strength attribute computed for the data. Bright spots correspond to the tracked horizons, these are the bands at 2.5 and above as seen on the color scale. Inset is the unmarked line

Variance in seismic traces is computed laterally to estimate differences and similarities in signal shape both in the inline and crossline direction. With the survey size available in this study, a window size of 5 yielded the desired smoothing effect that accentuated the edges of continuous reflectors. Since the prolific central portion of the data is fairly undeformed and with minimal curvatures, the variance attribute was not passed through a dip or azimuth guide filter for result enhancement (Rotimi, et al., 2014b). Mild structural features appear in the mid-section of the data with other chaotic segments identified on the flanks. Ant tracking was used to further investigate portions structurally disturbed in an attempt to reveal horizon continuity (Rotimi, et al., 2019).

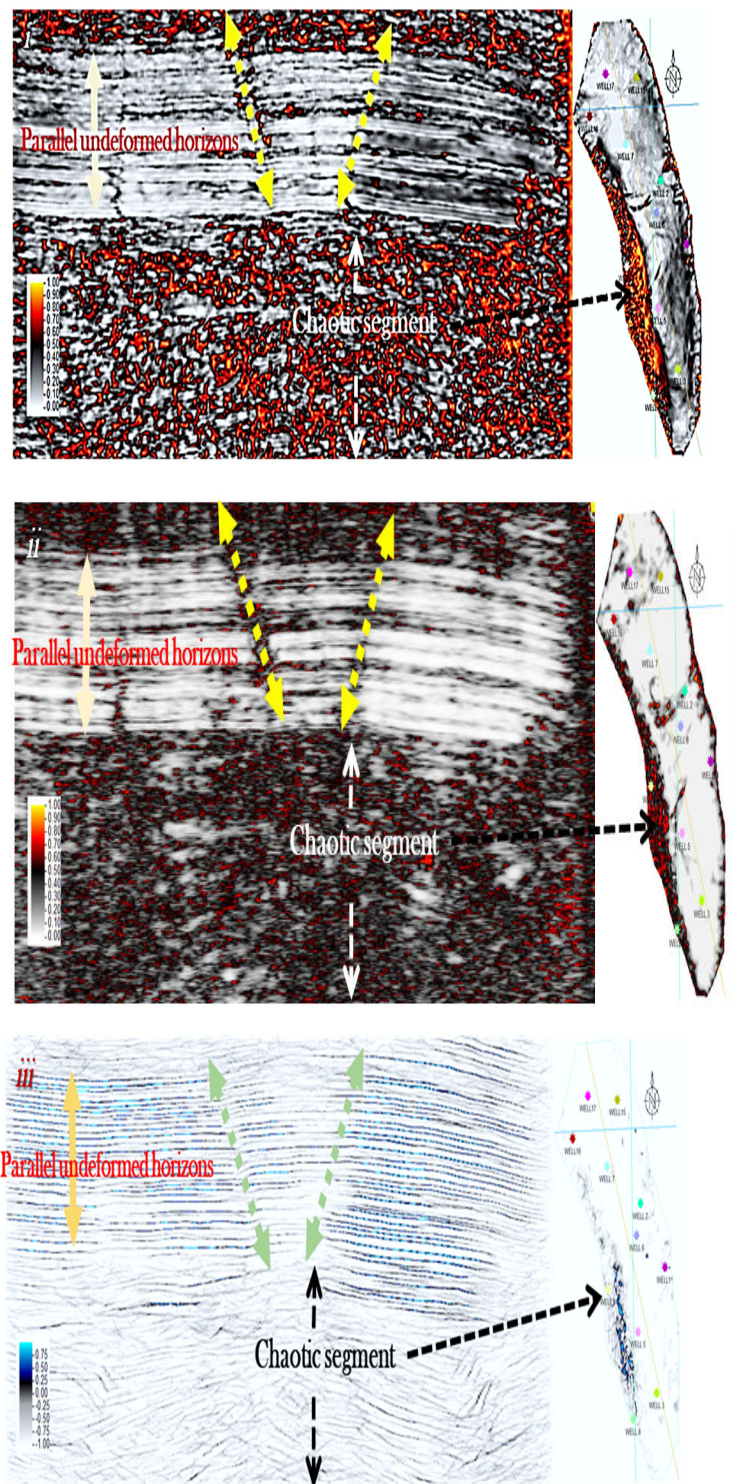


Figure 7: Computed attributes from seismic data showing parallel underformed formation in the upper part. Below this is the chaotic featureless segment. Slant lines with both 2 end arrows mark location with suspected fracture that seemingly separates the sequence in two. (i) Variance (ii) Chaos (iii) Ant tracking. Attribute captured around the horizon are presented on the right.

Acoustic Impedance (AI) Property Inversion

Petrel based inversion was done to derive rock properties from the seismic data. A Multi-layer neural network fused with genetic algorithm was used to achieve this. The Acoustic Impedance Inversion volume uses the Sonic and Density data as a priori (Brian Russell, 2019). Seismic data and computed Acoustic Impedance log were used as training data. The algorithm de-spikes the log for spurious records and applied low-pass frequency filter (Veeken *et al.*, 2009). The genetic algorithm back propagates the error and updates the weights for the neural network. With the genetic algorithm, convergence of the inversion towards achieving global stability and minimal error is greater than conventional neural networks even with characteristic seismic data density. Furthermore, this method is faster and can be used to invert for other petrophysical or elastic properties and other wave equation parameters. Minimum convergence percentage of 85 was used with 70 % of data was delineated for the data training purpose. The remaining 30 % was used to validate the process. 1500 maximum iteration was applied to handle the sample seismic volume used for training and TWTT constraints. This and the number of iteration impacts on the overall computation time. Figure 8 is the result of the inverted volume.

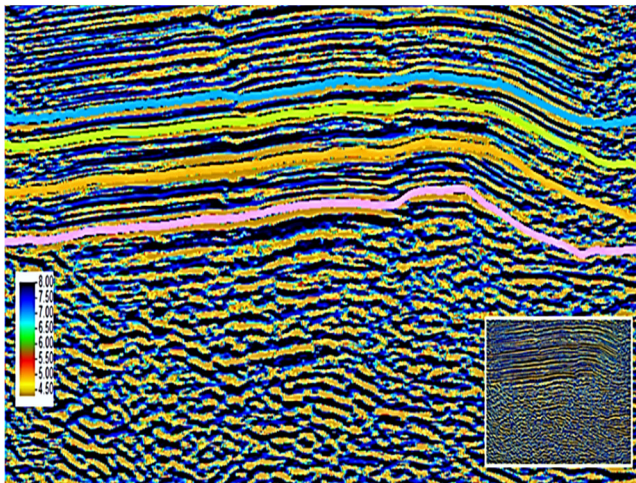


Figure 8: Acoustic impedance inversion result with tracked horizon shown. Inset is the untracked line.

A window of between 3 and 5 signal samples was adopted around which seismic attribute surfaces were built for each tracked horizon which initially followed signal trough. This was essentially done primarily for Acoustic impedance and Reflection strength which are stratigraphy enhancing attributes while those for the structural attributes were captured for validation of lateral variation in reflection characteristics across the field (Figure 7). Both stratigraphic attributes provide evidence for rock types and fluid hosting potential. Observed variation and description are presented in the result section.

3.0 Results and Discussion

The obtained properties are shown in table 1 and average values for the reservoirs were obtained by blocking the reservoir and averaging.

The average porosity is about 16 %, average water saturation is about 16 % and average permeability is approximately 25 md.

Surface attributes around tracked horizon are shown in figures 9 – 19. The hydrocarbon prolific zones occur at the center of the dome structure moving to the mid-section of the southern part. Acoustic impedance for this zone is not below 6.5. Most other parts flanking the dome corresponds to the chaotic segments with most prominent occurrence on the western part of the survey. This pattern is irregular and varies in intensity for all surfaces. It appears thinner in horizon 1 and 2 but broader in 3 and 4 (figure 9). This is arguably giving way for the proximal part of the domeless strained, unstable, and having dispersed sediments. This central portion with plain bright reflections is the most promising segment interpreted as the sand from AI value. The northern portion from horizon 3 and 4 appear brightest while a slight switch is noticed in horizon 4 corresponding to the proximal part of the dome. Figure 10, reflection strength surfaces, validates the inherent pattern of the AI result. The bright spot on the instantaneous amplitude grows from i - iv. Although, the portion reduces with corresponding increased brightness, figure 10(iii and iv), still have the most dominant bright spots across the dome. This remarkable trend is also seen in the well attribute surfaces presented in Figures 11 – 19. AI properties with values above 6.0 KPa.s/cm³ are interpreted as consisting of higher sand ratio of above 40 % and of higher density. Analysis of crossplot of Figure 3 is confirmed on the surfaces computed from the seismic data as seen in Figure 9, laterally distinguishing the lithologies. The density variation can be further inferred from the parallel nature of this horizon consisting of higher compressional wave velocity and Poisson ratio of between 0.3 and 0.47 (figure 3). Both plots show distinguished formations.

Poisson's ratio on the flanks is significantly lower on horizon 1 and 2 with higher variation on the northeast and southeast portion (figure 11). The value increases on the average with depth. Porosity value is lowest across all 4 horizons on the southeast segment (figure 12). The ubiquitous chaotic segment also appears highly porous especially in the western flank. This thus, replicates the earlier observed intrinsic directional variation in the dome structure. The water saturation is a very important and sensitive parameter in estimating volumes in place and reserves. Water saturations range from an average of 0.11 in well 5 and 0.50 across the field (figure 13). Horizon 1 reveals low water saturation in the upper segment but switches to the identified trend on horizon 2 – 4. This presents further discrepancy in water saturation across the area translating to the mid-section having the highest hydrocarbon saturation. Increased strain is observed in the central portion from the BI and E results (figure 14 - 15). Fluctuation of this property confirms the compressive nature of the structure and corresponding petrophysical properties. This central portion is the fairly parallel horizon having no distinct deformation element earlier presented (figure 7).

Permeability in the dome segment is classified fair to high (figure 16). Except horizon 1, the low permeability zones at the flanks of the dome correlates with the dispersed shale sediments. The northern part of horizon 1 is fairly fractured and probably accounts for the heightened

permeability value for this zone. This trend is also observed in the water saturation surface (figure 13). The trend pattern of the attribute property noticed on AI, V_p and V_p/V_s surfaces (figures 17 - 19) correlates with the defined structural configuration and validates lithology and identified porosity and fluid saturation indices.

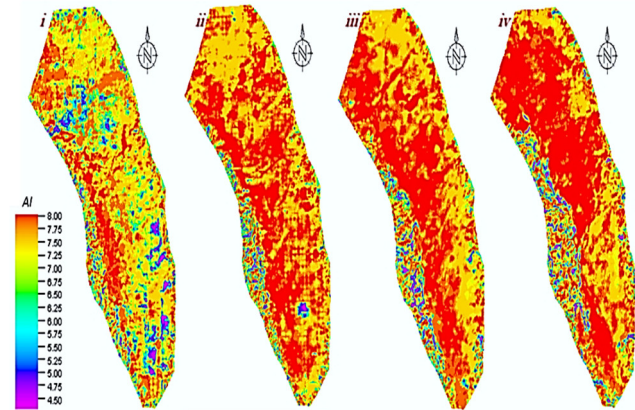


Figure 9: Acoustic impedance property surface captured around interpreted horizons (i - iv)

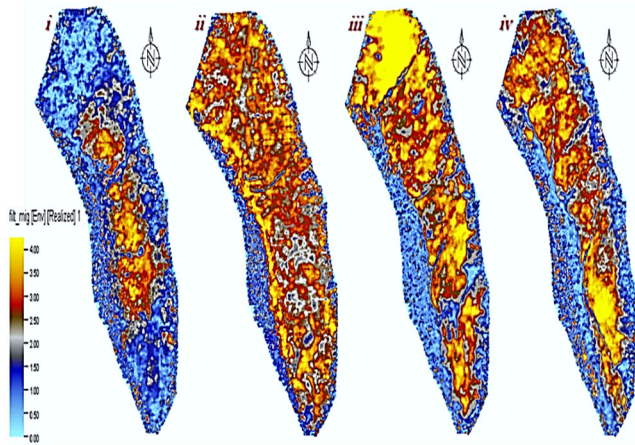


Figure 10: Reflection strength attribute over-interpreted horizon (i - iv). Bright spots indicate hydrocarbon presence.

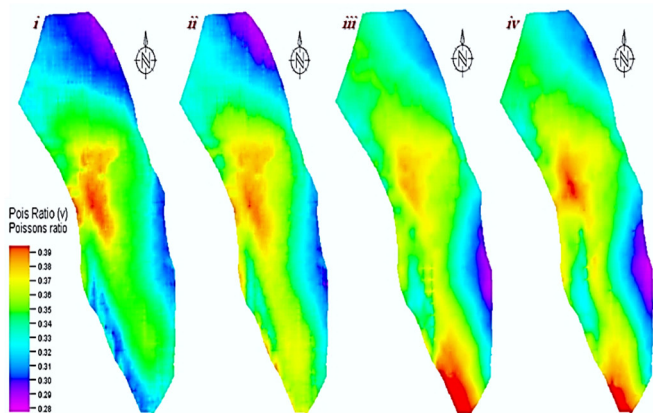


Figure 11: Poisson ratio surface for the interpreted horizons (i - iv)

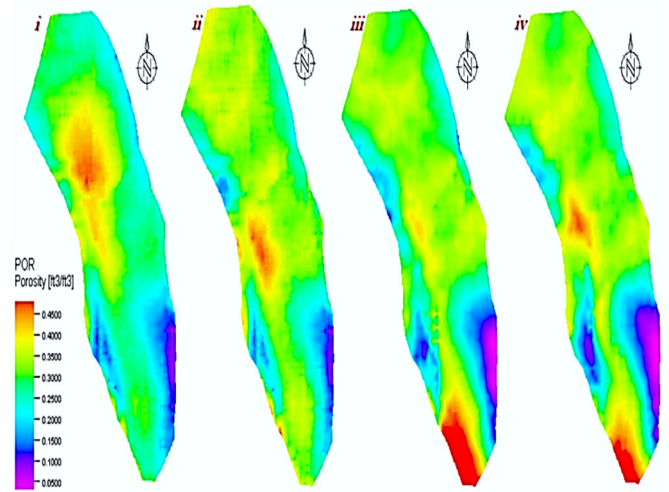


Figure 12: Porosity surface for the interpreted horizons (i - iv)

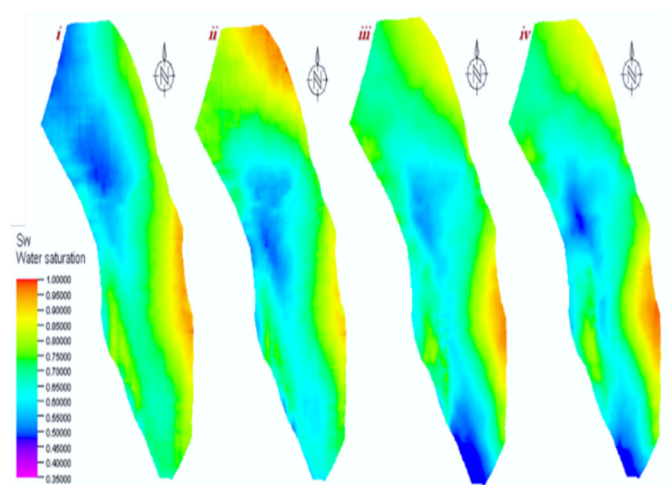


Figure 13: Water saturation surface for the interpreted horizons (i - iv)

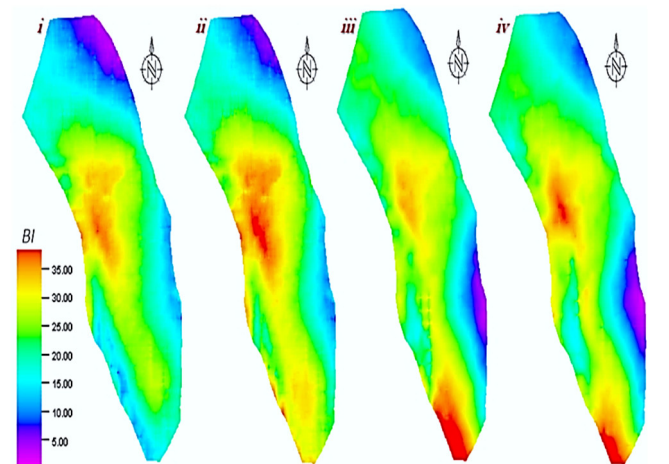


Figure 14: Brittleness index surface for the interpreted horizons (i - iv)

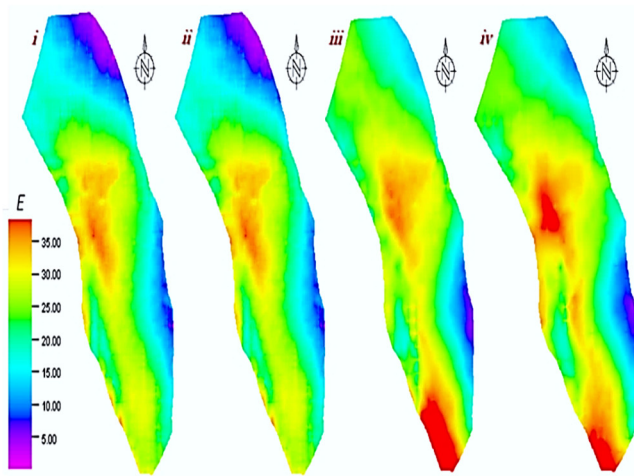


Figure 15: Young modulus surface for the interpreted horizons (i - iv)

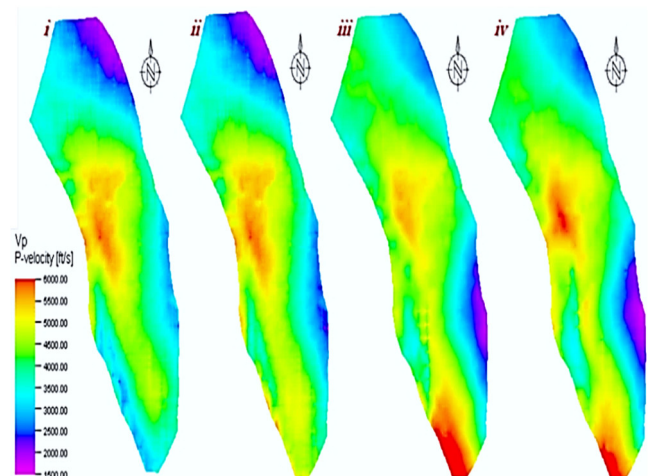


Figure 18: Compressional velocity surface for the interpreted horizons (i - iv)

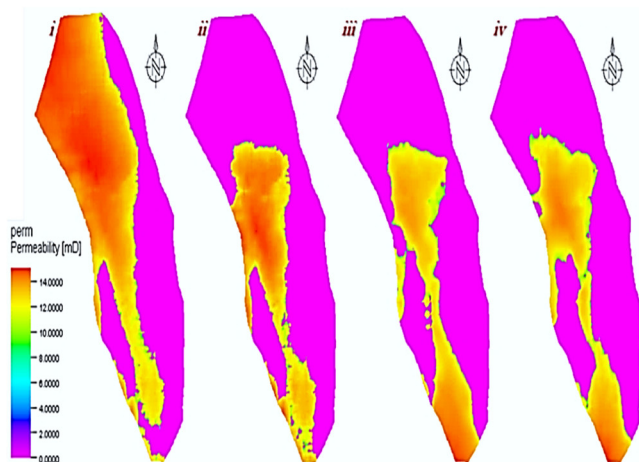


Figure 16: Permeability surface for the interpreted horizons (i - iv)

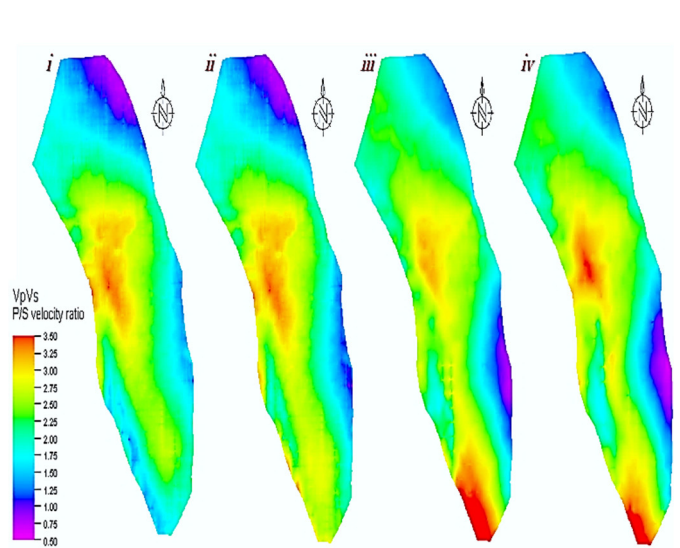


Figure 19: V_p - V_s ratio surface for the interpreted horizons (i - iv)

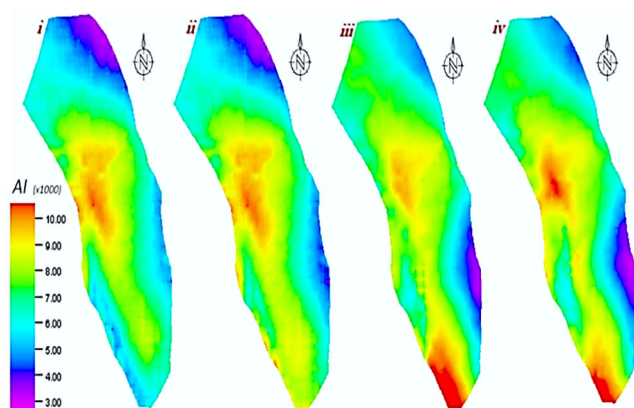


Figure 17: Acoustic impedance surface for the interpreted horizons (i - iv)

Variance surfaces

Between horizon 1 and 4, porosity variation shows higher porosity on the southeast portion. This part corresponds to the area with lower average V_p , BI and AI property value seen in figure 20. However, porosity for this segment is between 15 % and 25 % with the distal portion having significantly lower values. Conceptually, density variation increases with depth with prominent variation introduced by deformation, this pattern is seen replicated on the flank especially for most mechanical properties. This deformation often acts to alter expected trends in beds sequentially deposited and conformably stacked as the case of this area. This trend is sustained in other properties, suggesting a significant gravity-assisted compaction trend and fluid movement. This is properly captured by the permeability attribute surface shown. It gives a reasonable idea of the fluid movement interplay with mechanical property variation within the sequence and across the dome that was subjected to fair compressional deformational forces.

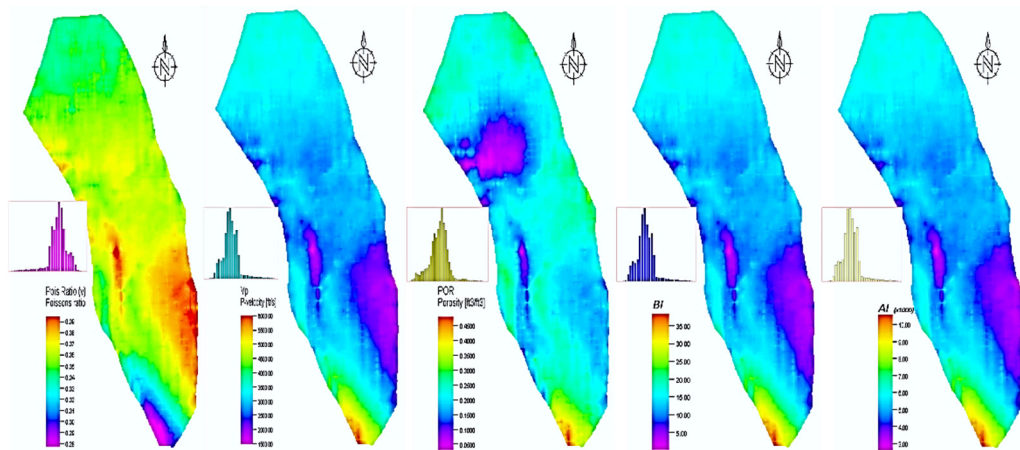


Figure 20: Petrophysical and elastic attributes variance surfaces for the interpreted horizons (i - iv)

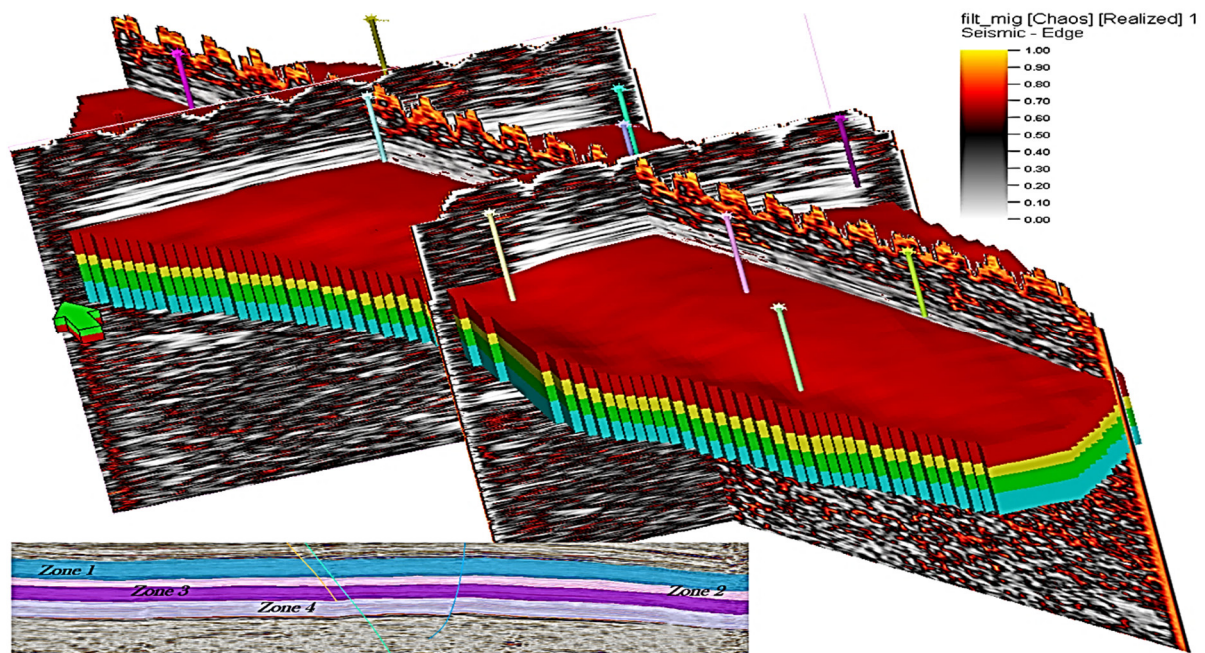


Figure 21: Structural modeling for the interpreted zones. Seismic lines are chaos and variance attributes. Wells 1 – 10 (shown in figure 1) are displayed penetrating the zones. Inset (profile on the southwest of the figure) is an intersection showing zones and suspected interpreted fractures.

Table 1: Summary of petrophysical and mechanical properties

Horizon	Average thickness	HC Type	Φ_E	S_w	S_h	K(md)	ν	G(Gpa)	Λ (Gpa)	AI	BI	E(Gpa)
1	603.44	oil	0.15	0.15	0.85	21.81	0.31	7.05	11.13	7800	25.73	28.15
2	566.27	gas	0.16	0.2	0.8	24.97	0.3	7.21	10.87	7780	25.8	28.32
3	469.2	oil	0.14	0.17	0.83	21.68	0.3	7.31	10.5	7770	25.32	28.74
4	391.96	oil	0.17	0.11	0.89	29.89	0.34	7.44	10.41	5440	22.85	24.28

Seismic facies control on properties is averred to significantly influence fluid property distribution in the dome and around it. Typical situation is noticed at the fringes of the dome which are characterized by chaotic reflections as against the crest part with more parallel reflections. The disordered portion has low Poisson's ratio value indicating their resistance to deformation as against the arched part with higher values. This arched part is interpreted as the deformed part with higher BI value. The implication is the tendency for this portion to fail under increased and unsupported stress from underlying strata which is also chaotic as the flanks are (Figures 7 and 21). This corresponds to E having greater rock stiffness value around the dome parts making it assume the current configuration in resisting uniaxial compression from the fringes. Most of the evaluated properties increases with depth in most direction. Water saturation partially varies with porosity for horizon 3 and 4. The variation of these properties for horizon 1 and 2 are higher especially in the upper half of the northern part. The part interpreted as stiff and liable to fail are partially porous and highly water saturated on the dipper horizons. The disordered parts are not as permeable as the stiffer arched crest part which is more permeable. Although this part is sufficiently strained, it is not structurally deformed as the flanks. High elastic constant and fluid properties characterize the dome part with alternating variations progressively radiating off towards the fringe.

Conclusion

Extensive petrophysical and mechanical evaluation of reservoir rocks identified 4 prolific hydrocarbon horizons with varying zone thickness. The following conclusions can be drawn:

1. Petrophysical parameters vary with reflection patterns. From wells interpreted, well top formations do not reflect lateral character away from the sampled wellbore position, until evaluated on seismic data. These properties (Φ , K and S_w), have higher values in the mid-portion interpreted as fairly parallel dome parts with continuous reflections.
2. Chaotic and parallel reflections are the two main facies recognized on the seismic data. The chaotic parts occurring at the flanks are not as stiff as the structurally bent dome part interpreted as stiffer arched segment and are often hydrocarbon saturated. Seismic attributes and Genetic inversion result suggests the mid-section as most prolific on both instantaneous amplitude and AI.
3. Elastic properties interpreted for the area spatially show varying values in different directions, especially V_p , V_s , E etc. Lower properties characterized the chaotic flanks while the arched mid-section is stiffer although it is due to the late deformation stage form.

Acknowledgement

The authors will like to acknowledge Rocky Mountain Oilfield Testing Center (RMOTC) and the U.S. Department of Energy as the data source, thank Covenant University for the support given for the study. MOST-CHINA is also appreciated for the equipment donated under the CASTEP scheme and used for this study. The efforts of the anonymous reviewers are appreciated.

Declaration of Conflict of Interests

The authors declare no conflict of interests.

Authors' Contributions

Conception: ROJ, OFT, EIF

Design: ROJ, EE, EIF, GCA

Interpretation: ROJ, OFT, OCY, AAA, EIF

Writing the paper: ROJ, OFT, EE, EIF, AGC

References

- Al-Kattan, W., Al-Ameri, J.N., 2012, Estimation of the Rock Mechanical Properties Using Conventional Log Data in North Rumaila Field. Iraqi Journal of Chemical and Petroleum Engineering, **13** (4): 28-33.
- Anderson, R.A., Ingram, D.S., Zanier, A.M., 1973, Determining Fracture Pressure Gradients from Well Logs. Journal of Petroleum Technology, **25** (11): 1259-1268.
- Bassiouni, Z., 1994, Theory, Measurement, and Interpretation of Well Logs. In Z. Bassiouni, Theory, Measurement and Interpretation of Well Logs. Richardson, Texas, USA: Society of Petroleum Engineers, **4**: 385.
- Bentley, L., Zhang, J., 2005, Factors determining Poisson Ratio. Crewes Report, **17**:1-15.
- Brian Russell, 2019, Machine learning and geophysical inversion - A numerical study. TLE, July Special Section: Machine learning applications. <https://doi.org/10.1190/tle38070512.1>. **38** (7): 512-519.
- Castagna, J., Greenberg, M.L., 1992, Shear velocity estimation in porous rocks: theoretical formulation, preliminary verification, and applications. Geophysical prospecting, **40** (2): 195-209.
- Chappelle, H.H., 1985, An analysis of the potential for enhanced oil recovery in the Shannon formation at Naval Petroleum Reserve #3. Naval Postgraduate school. Unpublished thesis. Pp. 372.
- Darling, T., 2005, Well, Logging and Formation Evaluation. <https://doi.org/10.1016/B978-0-7506-7883-4.X5000-1> Gulf Professional Publishing. Pp. 336.
- Edlmann, K., Somerville, J.M., Smart, B.G.D., Hamilton, S.A., Crawford, B.R., 1998, Predicting rock mechanical properties from wireline porosities. In Proceedings of the SPE/ISRM Rock Mechanics in Petroleum Engineering Conference Journal. <https://doi.org/doi:10.2118/47344-MS>. **2**:169-175
- Ellis, D.V., Singer, J.M., 2007, Well Logging for Earth Scientist (2nd ed.). Netherlands: Springer. Pp. 708.
- Fei, W., Huiyuan, B., Jun, Y., Yonghao, Z., 2016, Correlation of dynamic and static elastic parameters of rocks. EJGE, **21**: 1551-1552.
- Fjaer, E., Holt, R.M., Horsund, P., Raaen, A.M., Risnes, R., 2008, *Petroleum related rock mechanics*. Elsevier. 2nd Edition, **53**. Pp. 514.
- Friedmann, S. Julio, Stamp, Vicki W., 2006, Teapot Dome: Characterization of a CO₂-enhanced oil recovery and storage site in Eastern Wyoming. Environmental Geosciences, **13** (3): 181-199

- Huang, X., Betzler, C., Wu, S., Bernhardt, A., Eagles, G., Han, X., Hovland, M., 2020, First documentation of seismic stratigraphy and depositional signatures of Zhongsha atoll (Macclesfield Bank), South China Sea, Marine and Petroleum Geology, DOI: <https://doi.org/10.1016/j.marpetgeo.2020.104349>. **117**: 1-12.
- Jorg, H.V., Bottrill, A., Mildren, S., 2015, Uses and abuses of Brittleness Index with applications to hydraulic simulation. URTEC: 2172545. <https://doi.org/10.15530/urtec-2015-2172545.P.1-9>.
- Onyeji, J.A., Abdullahi, N.U., Owoyemi, B., Ekun, O.A., Akhigbemen, E., Ajaegwu, N., 2018, Coring Unconsolidated Formations under Challenging Drilling Conditions – A Case Study, Swamp- Niger Delta SPE-193457-MS. DOI - <https://doi.org/10.2118/193457-MS>. P.1-11.
- Krygowski, D., Asquith, G., 2004, *Basic Well Log Analysis* (2nd ed.). Methods in Exploration Series, No. 16, Pp. 224.
- Memarian, H., Azizi, V., 2006, Estimation of Geomechanical Parameters of Reservoir Rocks, Rock Mechanics in Underground Construction: ISRM International Symposium 2006: 4th Asian Rock Mechanics Symposium, 8-10 November 2006, Singapore, <https://doi.org/10.3997/2214-4609.201404063>.
- Mkinga, O., Joseph, E.S., Jon, K., 2020, Petrophysical interpretation in shaly sand formation of a gas field in Tanzania. Journal of Petroleum Exploration and Production Technology. 10. <https://doi.org/10.1007/s13202-019-00819-x>. **10**: 1201-1213.
- Nelson, R., 1962, Economic engineering analysis of the Shannon sand teapot dome, Natrona County, Wyoming. University of Texas. Pp. 216.
- Ricardo, G.G., 2005, Reservoir simulation of co2 sequestration and enhanced oil recovery in Tensleep Formation, Teapot Dome field. Master's thesis, Texas A&M University. Texas A&M University. Available electronically from <http://hdl.handle.net/1969.1/3083>.
- Rotimi O.J., Zhenli, W., Richard, O.A., 2016, Characterizing Geometrical Anisotropy of Petrophysical properties in the middle Shahejie formation, Liaohe Depression, China. International Journal of Applied Environmental Sciences (IJAES), **11** (1): 89-109
- Rotimi O.J., Zhenli W., Ako B.D., Uhuegbu C.C., 2014, Seismic attribute utilization for structural pattern detection, fault imaging and prospect identification. Journal of Petroleum & Coal, **56** (5): 532-543.
- Rotimi O.J., Ako B.D., Zhenli W., 2014, Application of Rock and Seismic Properties for Prediction of Hydrocarbon Potential. Journal of Petroleum & Coal. **56** (1): 40-53.
- Rotimi O.J., Ameloko A.A., Adeoye O.T., 2010, Applications of 3-D Structural Interpretation and Seismic Attribute Analysis to Hydrocarbon Prospecting over X – Field, Niger – Delta. International Journal of Basic & Applied Sciences IJBAS-IJENS, **10** (4): 28-40.
- Rotimi, O.J., Zhenli, W., Liang Y., 2019, Delineating fracture patterns from seismic and well derived multi-attributes data. <https://doi.org/10.2118/198763-MS>. Pp. 1-9.
- Terzaghi, K., Peck, R.B., Mesri, G., 1996, Soil mechanics in engineering practice. 3rd Edition, John Wiley & Sons. Pp. 592.
- Thomas, E.C., Stieber, S.J., 1975, Distribution of shale in sandstones and its effect upon porosity. In: SPWLA 16th annual logging symposium. New Orleans, Louisiana: SPWLA. [https://www.onepetro.org/conference-paper/SPWLA-1975-T.7\(18\):1-15](https://www.onepetro.org/conference-paper/SPWLA-1975-T.7(18):1-15).
- Veeken, C.H., Ivan, I.P., Leo, E.S., Yan, I.S., Alexander, Y.B., Yuri, P.A., 2009, Nonlinear multitrace genetic inversion applied on seismic data across the Shtokman field, offshore northern Russia. Geophysics, **74** (6): WCD49–WCD59. Doi. 10.1190/1.3223314.
- Xu, H., Zhou, W., Wie, R., Da, L., Xia, C., Shan, Y., Zhang, H., 2016, Characterization of rock mechanical properties using lab tests and numerical interpretation model of well logs. Mathematical Problems in Engineering. Hindawi Publishing cooperation. <https://doi.org/10.1155/2016/5967159>. **2016**:1-13.
- Zheng, J., Liange, Z., Hui-Hai, L., Yang, J., 2015, Relationships between permeability, porosity and effective stress for low-permeability sedimentary rock. International Journal of Rock Mechanics & Mining Sciences. DOI: 10.1016/j.ijrmms.2015.04.025. **78** (C): 304–318.